Acoustic holograms in contactless ultrasonic power transfer systems: Modeling and experiment

Marjan Bakhtiari-Nejad, Ahmed Elnahhas, Muhammad R. Hajj, and Shima Shahab

Citation: Journal of Applied Physics **124**, 244901 (2018); doi: 10.1063/1.5048601
View online: https://doi.org/10.1063/1.5048601
View Table of Contents: http://aip.scitation.org/toc/jap/124/24
Published by the American Institute of Physics

JOURNAL OF APPLIED PHYSICS **124**, 244901 (2018)

Acoustic holograms in contactless ultrasonic power transfer systems: Modeling and experiment

Marjan Bakhtiari-Nejad,[1] Ahmed Elnahhas,[2] Muhammad R. Hajj,[1] and Shima Shahab[1,a)]
[1]*Department of Biomedical Engineering and Mechanics, Virginia Tech, Blacksburg, Virginia 24061, USA*
[2]*Department of Mechanical Engineering, Virginia Tech, Blacksburg, Virginia 24061, USA*

(Received 16 July 2018; accepted 4 December 2018; published online 26 December 2018)

Contactless ultrasonic acoustic energy transfer (UAET) is a new technology that eliminates risks or impracticalities associated with wired electrical connections or batteries that need to be replaced on a regular basis. This technology, which is based on the reception of acoustic waves at ultrasonic frequencies by piezoelectric receivers, can be used to wirelessly charge low-power electronics. The execution and efficiency of this technology can be significantly enhanced through patterning and focusing of the transmitted acoustic energy in space to simultaneously power distributed sensors or devices. This work investigates the use of an acoustic hologram to create a multifocal pressure pattern in a plane where target receivers are located at specific focal points or regions. First, a phase-shifting hologram is designed using an iterative angular spectrum approach. Then, a multi-physics acoustic-electro-elastic model is presented for an axially vibrating cylindrical transmitter used to power multiple piezoelectric receivers, in conjunction with the hologram. Experiments are also performed to show the capability of an acoustic hologram to selectively power an array of the receivers. Both analytical and experimental results show a dramatic enhancement of power transfer to receivers exposed to a multi-focal pressure pattern created by the hologram. As a case study, a bi-focal receiver setup is investigated where one receiver is targeted. The UAET simulation predicts a doubling of the power transfer to the targeted receiver, which is verified by the proof-of-concept experiment. The effects of system parameters such as input frequency and hologram aperture size are also reported. *Published by AIP Publishing.* https://doi.org/10.1063/1.5048601

I. INTRODUCTION

The generation and control of three-dimensional sound fields is a long-standing problem, with applications that include ultrasound medical treatment (e.g., targeted drug delivery) and imaging,[1–3] energy transfer,[4] and particle manipulation.[5,6] Initially, acoustic manipulation was conducted using phased array transducers,[7–10] but the cost associated with active transducers and their phase-shifting circuitry was a deterrent for their implementation. Over the past decade, acoustic metamaterials have been investigated and characterized, with demonstrated effects such as beam-steering,[11–14] acoustic focusing,[15–18] multifocal focusing,[11,19,20] negative refraction,[12,21] broadband impedance matching,[22] analog computing,[23] and acoustic cloaking,[24] as well as passive acoustic holography,[11,19,20] which has attracted significant interest because it can be used to generate arbitrarily complex acoustic fields. Passive acoustic holograms store the phase and amplitude profile of a desired wavefront in a two-dimensional design which is used to reconstruct the acoustic pressure field when illuminated with a coherent acoustic source. These holograms can be implemented using one of two approaches, unit-based acoustic metamaterials such as labyrinthine cells,[11,19,20] and continuous three-dimensional printed phase-shifting lenses.[25–29] Both the acoustic metamaterial and three-dimensional printing implementation offer full phase control (0° to 360°), while only the acoustic metamaterials are capable of demodulating amplitude and phase controls.[11,20] However, the simplicity of design and fabrication of the three-dimensional printed holographic lenses allows for their implementation in applications such as particle manipulation[25] and optically generated ultrasound.[27–29]

During the same period, ultrasonic acoustic energy transfer (UAET) has emerged as a new approach for contactless energy transfer (CET). UAET relies on transferring energy using sound waves and is primarily implemented using piezoelectric (PZT) transmitters and receivers. Several proof-of-concept experiments have been conducted through different media reporting various efficiencies. A review highlighting major advancements is presented by Roes *et al.*[4] One of the challenges for enhancing wireless power transmission and selectively charging sensors or devices is patterning and focusing the transmitted acoustic energy in space. The localization of energy is important as it can be used for biomedical applications such as lithotripsy[30] (kidney stone removal) or more general applications such as efficiently powering sensor networks. Furthermore, there are scenarios where localizing the energy transfer is not only a desire but a must due to the delicacy of the system in which energy transfer is implemented. Such examples include sensor nodes[31] or neural dust sensing motes placed throughout the human brain.[32] One scenario is the use of high-intensity focused ultrasound (HIFU) technology[33] or acoustic mirroring concept[34–36] to focus the transmitted energy in space, and, thereby, strongly excite the receiver. However, focusing should obviously be carefully employed in UAET since HIFU may yield substantial energy localization and heating,[33] with levels that may not be allowable because safety regulations require

---

[a)]Author to whom correspondence should be addressed: sshahab@vt.edu

0021-8979/2018/124(24)/244901/12/$30.00

Published by AIP Publishing.

acoustic intensity that is lower than 94 mW/cm^2 and limit the operating frequency to 100 kHz.[37]

In this research, we investigate the capability of a 3D-printed acoustic hologram for contactless acoustic power transfer, and conduct both theoretical and experimental studies to prove the potential of this technology. To this end, we propose to combine UAET systems with the diffraction-limited acoustic holograms employing the customized fabrication procedure that was first presented by Melde *et al.*[25] We utilize an iterative angular spectrum approach (IASA)[38] to create desired acoustic pressure patterns for the hologram fabrication. The output pressure pattern is then used in conjunction with a distributed parameter piezoelectric model[34,39] to compute the power transfer to spatially-distributed 33-mode receivers. The effects of varying the excitation frequency and size of the hologram aperture on the target image resolution are investigated. Experiments are conducted to show the potential of an acoustic hologram in constructing a single acoustic focus to selectively power a piezoelectric receiver. In Sec. II, we develop the theoretical background and model for the proposed UAET-hologram system. Results from simulations performed using the derived model are presented in Sec. III. Details and results from experimental validation of the model and simulation are discussed in Sec. IV. A summary and conclusions are presented in Sec. V.

II. ANALYSIS

Figure 1(a) displays a schematic of an acoustic hologram combined with a UAET system, which includes an array of piezoelectric receivers placed in a target plane that are excited by an incident acoustic wave from a transmitter and manipulated by the hologram. Figure 1(b) shows a schematic of the continuum model used to analyze the voltage output from the receivers.

The transmission coefficient for a normal incident wave through multilayer systems was derived by Callens *et al.*[59] and Hill and Dardiry,[40] and is written as

$$T_n = \begin{bmatrix} \cos(k_n t_n) & jZ_n \sin(k_n t_n) \\ \dfrac{j\sin(k_n t_n)}{Z_n} & \cos(k_n t_n) \end{bmatrix}, \tag{1}$$

Here, T_n is the transfer matrix for the nth material layer with acoustic impedance Z_n and thickness t_n, with one of the layers being the acoustic hologram, and k_n is the wave number in the nth material. The equivalent transfer matrix for the $n-$ layer system is derived by defining $T^{eq} = T_1 T_2 \ldots T_{n-2}$. Hence, the resultant equivalent acoustic impedance is written as

$$Z^{eq} = \frac{T_{11}^{eq} Z_n + T_{12}^{eq}}{T_{21}^{eq} Z_n + T_{22}^{eq}}. \tag{2}$$

Having calculated the equivalent acoustic impedance, the reflection coefficient R_I can be derived by replacing the multilayered boundary system with an equivalent single boundary system to write[41]

$$R_I = \left| \frac{Z^{eq} - Z_1}{Z^{eq} + Z_1} \right|^2. \tag{3}$$

The transmission coefficient T_I is then derived as $T_I = 1 - R_I$.

Placing a hologram in the multilayer acoustic structure between the source (transmitter) and the target plane (four-layer system), we can calculate the transmission coefficient as

$$\begin{aligned} T_I(x,y)\big|_{\text{four-layer}} = 8Z_0^3Z_h^2Z_s/\{&4Z_0^3Z_h^2Z_s + 2(Z_0^6 + Z_h^4Z_s^2)\sin^2(k_0 d)\sin^2[k_h t(x,y)] \\ &+ (Z_0^3Z_h^3 + Z_0^3Z_hZ_s^2 - Z_0^5Z_h - Z_0Z_h^3Z_s^2)\sin(2k_0 d)\sin[2k_h t(x,y)] \\ &+ 2(Z_0^4Z_h^2 + Z_0^2Z_h^2Z_s^2)\cos^2[k_h t(x,y)] + 2(Z_0^2Z_h^4 + Z_0^4Z_s^2)\cos^2(k_0 d)\sin^2[k_h t(x,y)]\}, \end{aligned} \tag{4}$$

where $t(x,y)$ is the thickness of a pixel in the hologram plane at position (x,y) and d is the distance between the transmitter and the hologram as shown in Fig. 1(a), and k_0 and k_h are the wave numbers in the medium and in the hologram body, respectively. Moreover, in Eq. (4), Z_h, Z_0, and Z_s are the acoustic impedance of the hologram, medium, and transmitter, respectively. For any material m, the characteristic acoustic impedance is given by $Z_m = \rho_m c_m$, where ρ_m and c_m are, respectively, the material density and speed of sound. Equation (4) is derived using the aforementioned equivalent transfer matrix method in which $Z_1, Z_2 = Z_4$ and Z_3 correspond to $Z_s, Z_0,$ and Z_h, respectively.

Accordingly, if the acoustic hologram is mounted on the transmitter (three-layer system), the transmission coefficient is derived as

$$\begin{aligned} T_I(x,y)\big|_{\text{three-layer}} = 4Z_h^2Z_0Z_s/\{&(Z_h^2 + Z_0Z_s)^2\sin^2[k_h t(x,y)] \\ &+ Z_h^2(Z_0 + Z_s)^2\cos^2[k_h t(x,y)]\}. \end{aligned} \tag{5}$$

Similarly, Eq. (5) is derived using the equivalent transfer matrix method in which $Z_1, Z_2,$ and Z_3 correspond to $Z_s, Z_h,$ and Z_0, respectively. In this paper, we investigate employing the acoustic hologram, which is mounted on the transmitter, and we aim to determine the pressure field in the target plane where the receivers are located.

A. Acoustic wave propagation from transmitter and hologram

The acoustic pressure close to the transmitter, where the hologram is located, is calculated using the Fast Nearfield Method (FNM).[42,43] FNM is a simulation method that takes advantage of the one-dimensional integral approach to determine the pressure near acoustic sources. The integral is the simplified form of the Rayleigh–Sommerfeld diffraction formula[44] and accounts for a uniform surface velocity of the circular source.[45] To predict the acoustic far-field distribution,

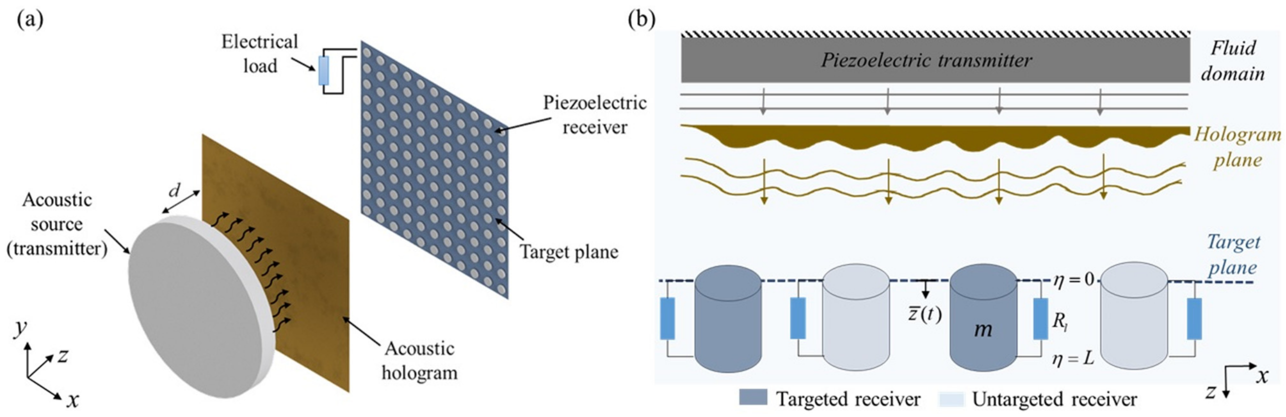

FIG. 1. Schematic representations of (a) an ultrasound energy transfer system with an acoustic hologram and (b) the longitudinal excitation of piezoelectric receivers (located in a target plane) by the transmitter and single acoustic hologram. Each receiver's axis of symmetry is perpendicular to the target plane.

we use the Angular Spectrum Approach (ASA) in which the complex acoustic pressure wave is represented as the summation of plane waves[46] and write

$$p_0(x, y, z = 0) = |p_0|(x, y, z = 0)e^{j\Delta\phi(x,y,z)} = \sum_{k_x}\sum_{k_y} P_0(k_x, k_y, z = 0)e^{j(k_x x + k_y y + k_z z)}, \quad (6)$$

where $|p_0|$ and $\Delta\phi$ are, respectively, the amplitude and relative phase of the complex input acoustic pressure and j is the unit imaginary number. The time dependency of $p_0(x, y, 0)$ is excluded for the sake of brevity. Equation (6) satisfies the Helmholtz equation $\nabla^2 p(\omega) + k^2 p(\omega) = 0$ in the frequency (ω) domain, providing that $k^2 = k_x^2 + k_y^2 + k_z^2$, where $k = \omega/c$ is the wave number and c is the speed of sound in the fluid domain. The angular spectrum of pressure wave at constant $z = 0$, $P_0(k_x, k_y, z = 0)$, is obtained from the two-dimensional Fourier transform as

$$P_0(k_x, k_y, 0) = \int_{-\infty}^{\infty}\int_{-\infty}^{\infty} p_0(x, y, 0)e^{-j(k_x x + k_y y)}dxdy. \quad (7)$$

The ASA computes the pressure at any arbitrary plane (target plane) using pressure field information at a parallel plane, e.g., $z = 0$ (hologram plane). Hence, when the angular spectrum of input pressure $P_0(k_x, k_y, 0)$ is identified, the angular spectrum at every parallel plane z is obtained as

$$P(k_x, k_y, z) = P_0(k_x, k_y, 0)H(k_x, k_y, z), \quad (8)$$

where $H(k_x, k_y, z)$ is the propagation function[47] written as

$$H(k_x, k_y, z) = e^{jk_z z}, \quad (9)$$

Hence, the pressure distribution at any desired (target) plane z is calculated using the inverse two-dimensional Fourier transform as

$$p(x, y, z) = \frac{1}{4\pi^2}\int_{-\infty}^{\infty}\int_{-\infty}^{\infty} P(k_x, k_y, z)e^{j(k_x x + k_y y)}dk_x dk_y. \quad (10)$$

Similarly, the ASA can be used to compute the backpropagation of the pressure field from the target plane to the hologram plane in which the corresponding angular spectrum at $z = 0$ is calculated as

$$P_0(k_x, k_y, 0) = P(k_x, k_y, z)H(k_x, k_y, -z), \quad (11)$$

where $H(k_x, k_y, -z)$ is the backpropagation function written as $H(k_x, k_y, -z) = e^{-jk_z z}$.

The ASA theory explained in this section is employed for the Near-field Acoustic Holography (NAH) method. The NAH is a technique that has been used for sound source identification,[48–52] and it is particularly effective for an inverse problem, i.e., backpropagation of the sound pressure from a target plane to a plane close to the acoustic source. NAH constructs the pressure field in a plane, as well as the fluid velocity and acoustic intensity vectors based on the pressure information of a parallel plane.[46] In this paper, by using the NAH, we show the capability to design an acoustic hologram to focus the acoustic energy in a desired pattern. The procedure will be explained in Secs. II B and II C.

B. Iterative angular spectrum approach algorithm

To obtain the desired acoustic pressure pattern in the target plane, the Iterative Angular Spectrum Approach (IASA) is used. Implementing the IASA starts by specifying the desired constraints, i.e., boundary conditions in the hologram plane and target plane.[25] Initially, the pressure field in the hologram plane (close to the transmitter) is computed via the FNM, and the phase distribution is set to zero. In the target plane, upon calculating forward-propagated pressure field via the ASA, we impose the desired target image amplitude on the field without changing the phase. Again, the pressure field in the hologram plane is computed via backpropagation of the wave from the target plane to the hologram plane. Then, the acoustic pressure amplitude of the hologram plane is set to that of the initial pressure amplitude (close to the transmitter) while considering the transmission losses, $|p_h(x, y, 0)| = \sqrt{T_I(x, y)}|p_0(x, y, 0)|$, and preserving the backpropagated phase. The IASA is repeated until the acoustic pressure field in the target plane converges to the desired target image, which in turn leads to the construction of the final thickness map of the hologram plate.

Additionally, we note that multiple forward and backward propagations of the acoustic filed lead to the reflection of higher spatial frequencies.[25] Therefore, we extend our computational domain in the x-y plane to at least three times the diameter of the transmitter and impose zero pressure outside the hologram area.

The thickness change of each pixel of the hologram (from the initial thickness of the hologram plate t_0) neglecting shear waves and attenuation is estimated as

$$\Delta t(x, y) = \frac{\Delta\phi_h(x, y)}{k_0 - k_h}, \qquad (12)$$

where $\Delta\phi_h(x, y)$ is the relative phase map calculated in the hologram plane and $\Delta t(x, y) = t_0 - t(x, y)$.

In summary, the IASA algorithm[25,38] used to design the acoustic hologram consists of the following steps:

1. The initial acoustic pressure amplitude $|p_0(x, y, 0)|$ is computed via the FNM at the hologram plane close to the transmitter face, and the phase map is set to zero.
2. The complex acoustic pressure in the desired target plane $p_t(x, y, z)$ is computed via the ASA using the propagation function.
3. The propagated pressure field is then compared to that of the target image.
4. If the comparison is satisfactory, the IASA is complete; otherwise, the acoustic pressure amplitude in the target plane is set to that of the desired target amplitude and the forward-propagated phase remains unchanged.
5. The imposed field is backpropagated to the hologram plane via the ASA using the backpropagation function.
6. The thickness map of the hologram and transmission coefficient are calculated.
7. The backpropagated acoustic pressure amplitude in the hologram plane $|p_h(x, y, 0)|$ is again set to the amplitude of the initial pressure field near the transmitter, and the transmission losses are applied [Eq. (5)]. The backpropagated phase remains unchanged.
8. The process is repeated from step 2 until a satisfactory distribution is obtained.

C. Acoustic propagation and piezoelectric receivers coupling in UAET: Closed-form voltage response at the steady state

The receiver disks in the target plane are free-free PZT cylinders operating in the 33-mode of piezoelectricity with fundamental resonance frequencies above the human audible frequency range [see Fig. 1(b)]. For the fluid-loaded and electrically-loaded free-free piezoelectric receiver disk excited by the acoustic wave, the coupled partial differential equations for longitudinal vibrations of the receivers and the AC electrical circuit are given by[34,39,53]

$$\begin{aligned} &-EA\frac{\partial^2 w(\eta, t)}{\partial \eta^2} - c_\gamma \frac{\partial^3 w(\eta, t)}{\partial \eta^2 \partial t} + \{c_\mu + R_r[\delta(\eta) + \delta(\eta - L)]\}\frac{\partial w(\eta, t)}{\partial t} \\ &+ m\frac{\partial^2 w(\eta, t)}{\partial t^2} - \kappa v(t)[\delta(\eta - L) - \delta(\eta)] = f_{top}(t)[\delta(\eta)] - f_{bottom}(t - \tau)[\delta(\eta - L)], \end{aligned} \qquad (13)$$

$$C_p\frac{dv(t)}{dt} + \frac{v(t)}{R_l} + \int_0^L \kappa \frac{\partial^2 w(\eta, t)}{\partial t \partial \eta} d\eta = 0, \qquad (14)$$

where $w(\eta, t)$ is the displacement response of the disk at the axial position η and time t, $v(t)$ is the voltage output across the electrical load, E is Young's modulus at constant electric field, A is the cross-sectional area, m is the mass per unit length, c_γ is the stiffness-proportional damping coefficient, c_μ is the mass-proportional damping coefficient, κ is the electromechanical coupling term in physical coordinates, and $\delta(\eta)$ is the Dirac delta function. The parameters C_p and R_l, respectively, represent the internal capacitance of the piezoelectric receivers and the external load resistance. The excitation forces due to the incident acoustic pressure, $f_{top}(t) = p_t(t)A$ at $\eta = 0$ and $f_{bottom}(t - \tau) = \beta p_t(t - \tau)A$ at $\eta = L$, given in terms of the acoustic pressure in the target plane $p_t(t)$ (see Sec. II B), are evaluated at the top surface ($\eta = 0$) and the bottom surface ($\eta = L$) of the receivers, where β is the ratio of the acoustic pressure on the bottom surface to that on the top surface and τ is the time delay of f_{bottom} relative to f_{top}. Moreover, the dissipative term R_r in Eq. (13) is the resistive component of the fluid radiation impedance (see Fig. 10.19 in Ref. 54). The excitation of the receiver is such that the linear piezoelectricity is assumed and the elastic coupling and dissipative nonlinearities are not prominent. The linear displacement at the free end of the piezoelectric receiver disk [$\bar{z}(t)$ in Fig. 1(b), where $\bar{z}(t) = w(0, t)$] due to harmonic excitation at or around the fundamental longitudinal (axial) vibration mode is obtained by modal analysis of the distributed-parameter electromechanical system for the fundamental mode of vibration. The longitudinal tip displacement of the piezoelectric receiver disk at time t is then written as

$$\bar{z}(t) = w(\eta, t)\big|_{\eta=0} = \varphi(0)\chi(t), \qquad (15)$$

where $\varphi(0)$ and $\chi(t)$ are the mass-normalized eigenfunction evaluated at $\eta = 0$ [Fig. 1(b)] and the generalized modal coordinate for the longitudinal vibration mode of a free-free uniform disk, respectively. The mass normalized elastic-mode eigenfunction, calculated from the corresponding undamped and electromechanically uncoupled (short-circuit) free vibration, is obtained as[34]

$$\varphi(\eta) = \left[\cos\,(\alpha\eta/L) - \alpha\frac{m_r}{mL}\sin\,(\alpha\eta/L)\right] \times \left\{\int_0^L m\left[\cos\,(\alpha\eta/L) - \alpha\frac{m_r}{mL}\sin\,(\alpha\eta/L)\right]^2 d\eta + m_r\left[\cos\,(\alpha) - \alpha\frac{m_r}{mL}\sin\,(\alpha)\right]^2 + m_r\right\}^{-1/2}, \tag{16}$$

where the eigenvalue, α, of the fundamental mode is the first non-zero root of the transcendental equation $[\alpha^2(m_r/mL)^2 - 1]\sin\alpha - 2\alpha(m_r/mL)\cos\,(\alpha) = 0$, where $m_r = X_r/\omega$ is the radiation mass, i.e., added mass, due to reactive component of fluid radiation impedance X_r (see Fig. 10.19 in Ref. 54) and ω is the excitation frequency.

The electromechanically coupled equations of forced vibration and current balance for the fundamental mode in the lumped-parameter form (reduced from distributed-parameter solution) are expressed as

$$\ddot{\bar{z}}(t) + [2\zeta\omega_n + R_r\varphi^2(0) + R_r\varphi^2(L)]\dot{\bar{z}}(t) + \omega_n^2\bar{z}(t) - \kappa[\varphi(0)\varphi(L) - \varphi^2(0)]v(t) = [f_{top}(t)\varphi(0) - f_{bottom}(t-\tau)\varphi(L)]\varphi(0), \tag{17}$$

$$[C_p\dot{v}(t) + v(t)/R_l]\varphi(0) + \kappa\,[\varphi(L) - \varphi(0)]\dot{\bar{z}}(t) = 0, \tag{18}$$

where the over-dot represents differentiation with respect to time and ζ is the damping ratio.[55] Here, acoustic absorption, nonlinearity, and scattering effects are assumed to be negligible for the frequency range of interest and receiver dimensions.

The steady-state electromechanical response to harmonic excitation is also harmonic and is of the form $\bar{z}(t) = |\bar{z}|e^{j\omega t}$ and $v(t) = |v|e^{j\omega t}$ based on the linear system assumption. Here, $|\bar{z}|$ and $|v|$ denote amplitudes of the axial displacement and voltage output, respectively. As a result, the fundamental-mode output voltage amplitude frequency response function (FRF) is obtained as[34]

$$|v| = \left|\frac{j\omega\kappa|p_t|A\left[\varphi(0) - \beta\varphi(L)e^{-j\psi}\right]\left[\varphi(0) - \varphi(L)\right]}{\left\{\omega_n^2 - \omega^2 + j\omega\left[2\zeta\omega_n + R_r\left(\varphi^2(0) + \varphi^2(L)\right)\right]\right\}\left(1/R_l(\omega) + j\omega C_p\right) + j\omega\kappa^2\left[\varphi(L) - \varphi(0)\right]^2}\right|, \tag{19}$$

where $\psi = \omega\tau$ is the phase angle between the excitation forces at the top and bottom surfaces of the cylindrical receivers. Consequently, the power output FRF of the piezoelectric receiver disks (Π) is calculated using the equation $\Pi = v^2/R_l$.

As a new method, combining the developed piezoelectric-based UAET formulations with the acoustic holography technique, imposing constraints on the amplitude of pressure distribution in the target plane, enables us to construct a desired multi-focal acoustic field where power transmission to receivers are focally achieved and enhanced dramatically. The analysis presented in this section starts with defining a desired pressure pattern in the target plane where multiple receivers are placed. Then, by applying acoustic holography, the thickness map of a hologram is determined. This map is used to form the hologram. The combination of the acoustic source and designed hologram enables selective powering of the piezoelectric cylindrical receivers. We expect that the developed theory for using holograms in contactless transfer of acoustic power will provide new insights into applications of UAET.

III. THEORETICAL RESULTS

A. Acoustic pressure distributions and the thickness map of the hologram

In this section, the numerical simulation of constructing the pressure fields and hence obtaining the information needed for fabrication of an acoustic hologram is illustrated. Having computed the initial pressure field close to the face of the circular transmitter using the FNM at 1 MHz, the ASA is used to compute the pressure field in the target plane at $z = 50$ mm in water domain. The operating frequency of 1 MHz is selected to achieve the reasonable solution quality (the effects of different frequencies are explored in Sec. III C), and the target depth of 50 mm is a common depth in UAET applications. The acoustic hologram is numerically designed to be driven by a piezo transducer disk with a diameter of 100 mm. Figure 2 shows the pressure distributions after 50 iterations obtained by implementing the IASA algorithm in Sec. II B. In Figs. 2(a) and 2(b), the amplitude and phase of the backpropagated final pressure distribution in the hologram plane, p_h, after transmission through the hologram (step 7 in the IASA algorithm) are shown. The resultant amplitude and phase of the pressure field p_t at the target plane are, respectively, shown in Figs. 2(c) and 2(d). The pressure field p_t in the target plane results from step 4 in the IASA algorithm, which converges to the target image when the IASA is complete. Here, we have chosen the university logo, VT shape, as the target image in order to show the potential of the computational simulation to reconstruct the complex pressure pattern. The resultant acoustic pressure distribution matches well with the VT shape desired pattern that we imposed upon the target plane, which shows the capability of

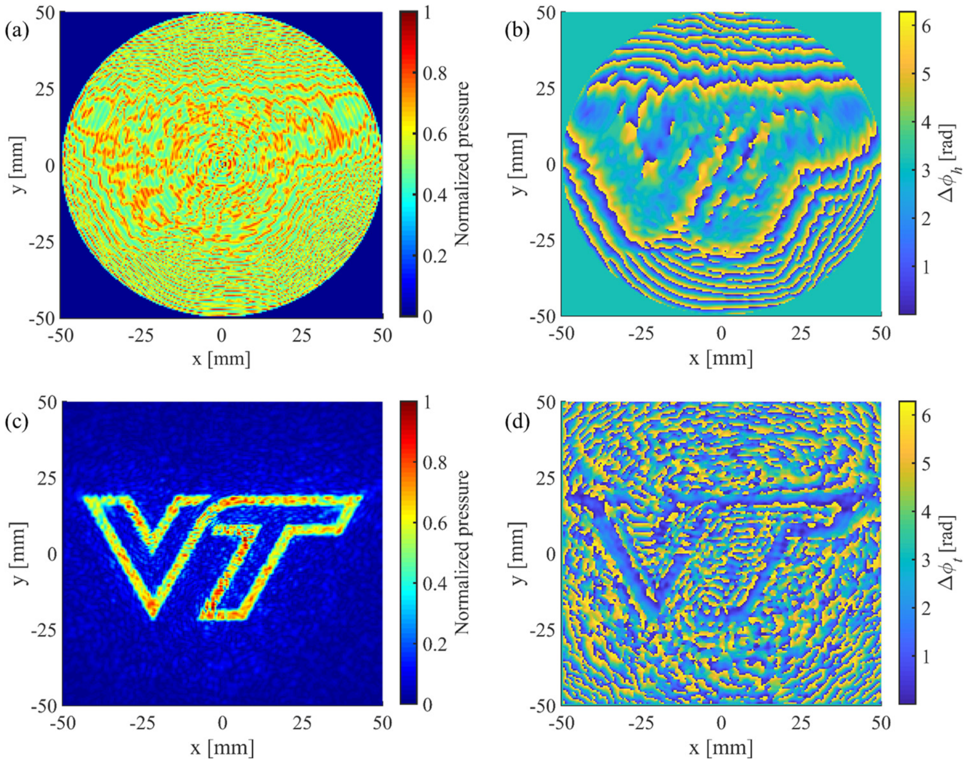

FIG. 2. Acoustic pressure distribution in the hologram plane close to the transmitter face, after transmission through the acoustic hologram: the (a) amplitude and (b) relative phase. Resultant propagated pressure field in the target plane at $z = 50$ mm: the (c) amplitude and (d) relative phase. The driving frequency is 1 MHz.

the designed hologram in multi-focal lensing and acoustic pressure transmission to generate higher amplitudes over specified patterned areas, compared to the case in which there is no hologram. The comparison indicates about 32% increase in the average acoustic pressure. In this simulation, the number of pixels associated with the diffraction-limited acoustic hologram is 201×201 with a resolution of $\lambda/3$ where λ is the wavelength, and the computational domain size is 601×601.

The final thickness map of the hologram is then computed using the final relative phase map [Fig. 2(b) and Eq. (12)]. Figure 3(a) illustrates this map, with the initial thickness of 5 mm, which is later used as an input to the 3D printer for the fabrication of the hologram shown in Fig. 3(b). The hologram was printed with a 3D printer (Form 2, Formlabs) using Clear Resin material with a resolution of 50 μm. The simulations were performed using the properties for water and axially vibrating cylindrical PZT transmitter with the density of 1000 kg/m^3 and 7800 kg/m^3 and the speed of sound of 1500 m/s and 4000 m/s, respectively. Moreover, the hologram properties were set to 1100 kg/m^3 for the density and 2424 m/s for the speed of sound in the material.

B. Receivers' power output in the target plane

In this section, the receivers' power output in the target plane is calculated using the obtained pressure distribution in the plane, where 1024 PZT receivers were equally distributed. Each receiver investigated in this case study is a cylindrical 33-mode PZT disk [PIC 255 from Physik Instrumente (PI) GmbH & Co. KG[56]] with a diameter of 3 mm and a thickness of 2 mm, and a short-circuit fundamental resonance frequency of 1 MHz in free-free boundary conditions. The material properties are given by the manufacturer in Ref. 57. The whole setup (in Fig. 1) is submerged under water. Using the analytical model, further simulations were conducted to

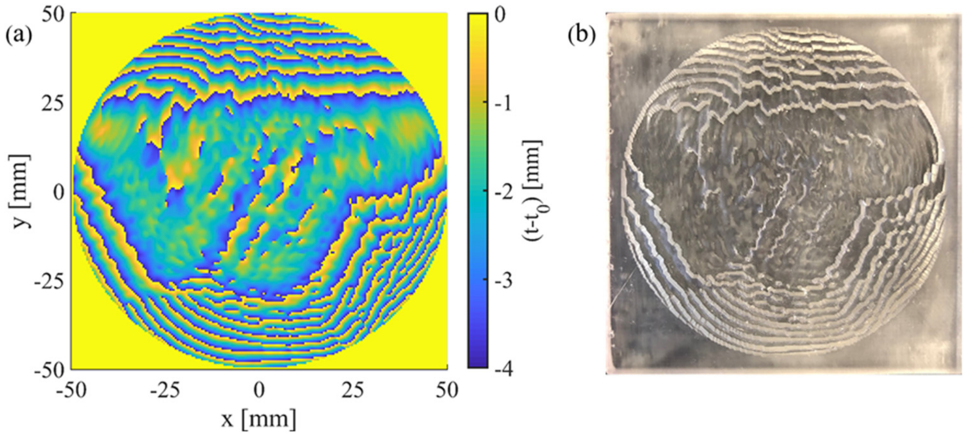

FIG. 3. (a) Final thickness map of the hologram plate operating at 1 MHz obtained from the IASA and (b) the 3D-printed hologram plate.

obtain the electrical power output for the PZT receivers in the target plane at $z = 50$ mm for two cases, i.e., with and without the hologram. The power output for the receivers is calculated at 1.08 MHz, the underwater open-circuit resonance frequency, and the load resistance is fixed to $R_l = 12\,\mathrm{k}\Omega$ (see Fig. 3 in Ref. 58). The pressure amplitude in the target plane at each receiver's location is used to calculate the external force acting on the surfaces of the receiver and is used in Eq. (19) to compute the output voltage amplitude from each receiver. This voltage is used in conjunction with the electrical load to calculate the power output. Since the pressure distribution over the surface of each receiver is not uniform, the pressure field in the target plane is divided into a coarser grid that has the nominal dimension of the diameter of the receivers. The pressure over each grid point is then averaged and is multiplied by the receiver area to estimate the external force over each receiver's surfaces.

Figures 4(a) and 4(b) show the normalized pressure distribution in the target plane when there is no acoustic hologram and in the presence of the hologram, respectively. Correspondingly, the normalized power output without the presence of the hologram is shown in Fig. 4(c), while Fig. 4(d) shows the normalized power output using the acoustic hologram. The figures depict an array of receivers that covers the domain in the target plane corresponding to the hologram aperture. It is determined that the acoustic hologram enables a new capability in shaping the acoustic pressure field and transferring power to the receivers only at focal points (in the VT pressure pattern) selectively. For this case study, in addition to patterning, employing the hologram in the UAET setup leads to a 9% increase in the average power output. Furthermore, Fig. 4(d) shows that the receiver with the highest power or normalized power output equals to 1, when the acoustic hologram was used, is located at $x = -22.5$ and $y = -16.5$ mm in the target plane. Comparing with the corresponding receiver in the same location, where the normalized power output equals to 0.33 without employing a hologram [Fig. 4(c)], the receiver's power output was increased by 200%. The power can be further increased with impedance mismatch alleviation and the inclusion of impedance-matching layers between the transmitter, hologram, and receivers.[59]

C. Effects of various parameters on pressure pattern in the target plane and thickness map of the hologram

In this section, we aim to analyze the effects of various parameters on the reconstruction of the target pressure pattern and fabrication of the hologram plate via its thickness map. The propagated pressure fields in the target plane at $z = 50$ mm for six different operating frequencies, namely 100 kHz, 250 kHz, 500 kHz, 1.5 MHz, 2.5 MHz, and 3.3 MHz, are shown in Fig. 5. The aforementioned frequencies were selected to visualize the effects of operating frequencies on the fidelity of the system. Moreover, there is a limit for the ASA to which the frequency can be increased depending on the distance from the hologram plane to the target plane and also on the desired pattern. For our case study, the frequency cannot be increased more than 3.3 MHz (with a $\lambda/2$ sampling criteria to avoid aliasing); however, at a smaller distance, e.g., $z = 20$ mm, the hologram can be constructed at much higher frequencies such as 7 MHz or above. Comparing the results obtained in Fig. 2(c) at 1 MHz and Figs. 5(a)–5(c), it is concluded that the hologram potential in generating the desired pressure pattern and hence performance quality and accuracy decrease as the frequency is decreased. On the other hand, Figs. 5(d)–5(f) illustrate that increasing the frequency from 1 MHz to 1.5-3.3 MHz significantly improves the quality and

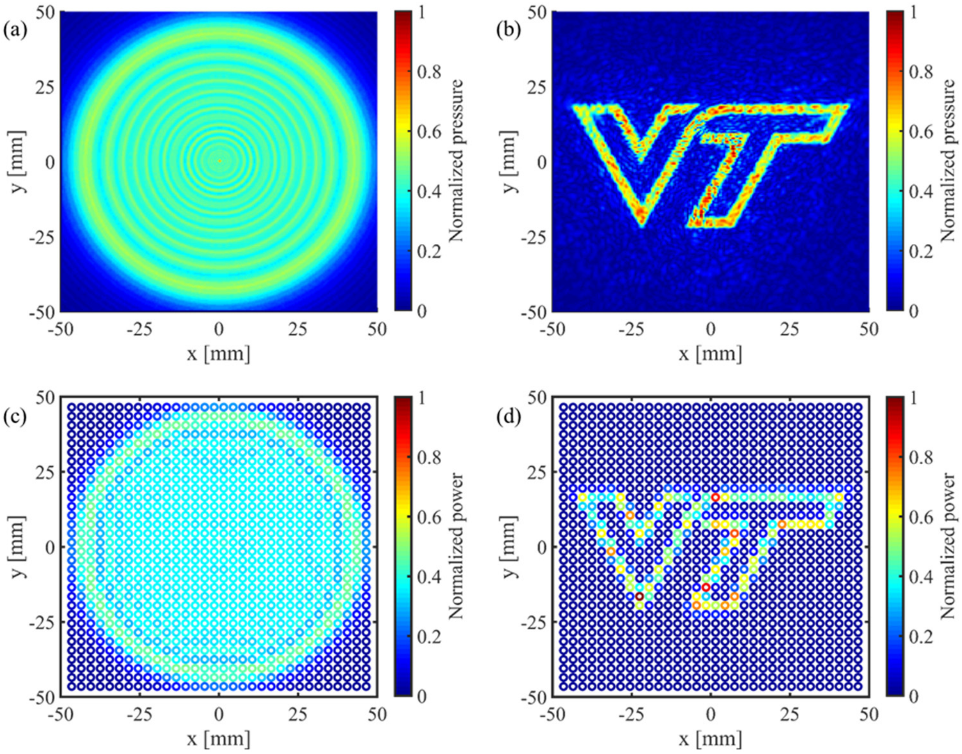

FIG. 4. Acoustic pressure distribution in the target plane at $z = 50$ mm: (a) when there is no acoustic hologram and (b) in the presence of the hologram. Power output for the piezoelectric receivers in the target plane at $z = 50$ mm: (c) when there is no hologram and (d) in the presence of the hologram. The pressure and power output are, respectively, normalized by the maximum value in (b) and (d), respectively.

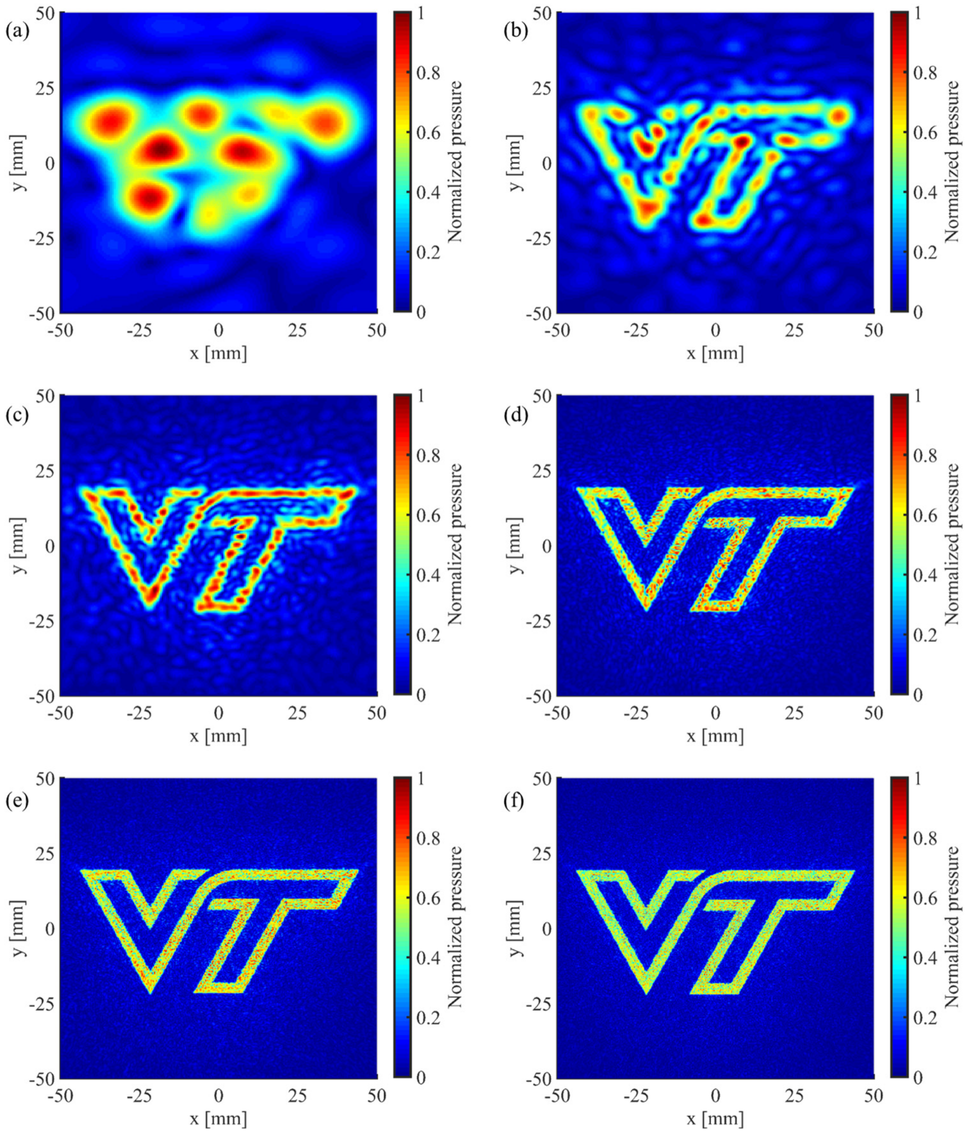

FIG. 5. Propagated pressure field in the target plane at $z = 50$ mm for excitation frequencies of (a) 100 kHz, (b) 250 kHz, (c) 500 kHz, (d) 1.5 MHz, (e) 2.5 MHz, and (f) 3.3 MHz.

uniformity of the patterned distribution of pressure in the target plane. Hence, increasing the operating frequency enhances the efficiency of the power transfer. Considering the corresponding thickness maps of the hologram that are shown in Fig. 6, we note that the resultant thickness map from the IASA before 3D printing is considerably affected by the excitation frequency. Apparently, over the frequency range below 1 MHz [Figs. 6(a)–6(c)], a low-quality designed thickness map is obtained which in turn leads to fabrication of imperfect hologram plate; thus, it generates a pressure pattern with less consistency in comparison to the desired target VT pattern. In contrast, Figs. 6(d)–6(f) show considerable improvements in the quality of the construction of desired holographic design when operating at 1.5-3.3 MHz with a more detailed structure of the pattern in comparison with the pattern of Fig. 3(a) at 1 MHz. Furthermore, at higher frequencies, the hologram plate can begin with smaller initial thickness since it requires less amount of maximum material removal, which results in a more consistent thickness map for the pixels of the hologram with a lower acoustic attenuation. This is one of the important features in making a consistent desired pattern since in a holographic technique, each pixel of the hologram acts as a single transducer in transmitting the acoustic field.

Likewise, we investigated the effects of various hologram aperture size and diameter of the PZT transducer disk. The results show that using a larger disk/aperture size will improve the quality of the hologram design and therefore enhance the reconstruction quality of the pressure pattern as well as the designed thickness map. For that, as an alternative, we suggest using an equivalent source method (ESM) for NAH that can administer sources with arbitrary geometry, i.e., the multi-aperture acoustic holography method.[48,60,61] The results of changing the aperture size are not presented for the sake of brevity, as they are analogous to those regarding the effects of changing the frequency. An example of transmission coefficient variation for three layers versus operating frequency and a layer thickness for different frequencies are shown in Figs. S1(a) and S1(b) in the supplementary material, respectively. Also, the calculated transmission coefficient in the hologram plane at 1 MHz for the computational case study is shown in Fig. S1(c).

The resolutions for each frequency in the simulations are chosen to ensure that a reasonable solution quality, which

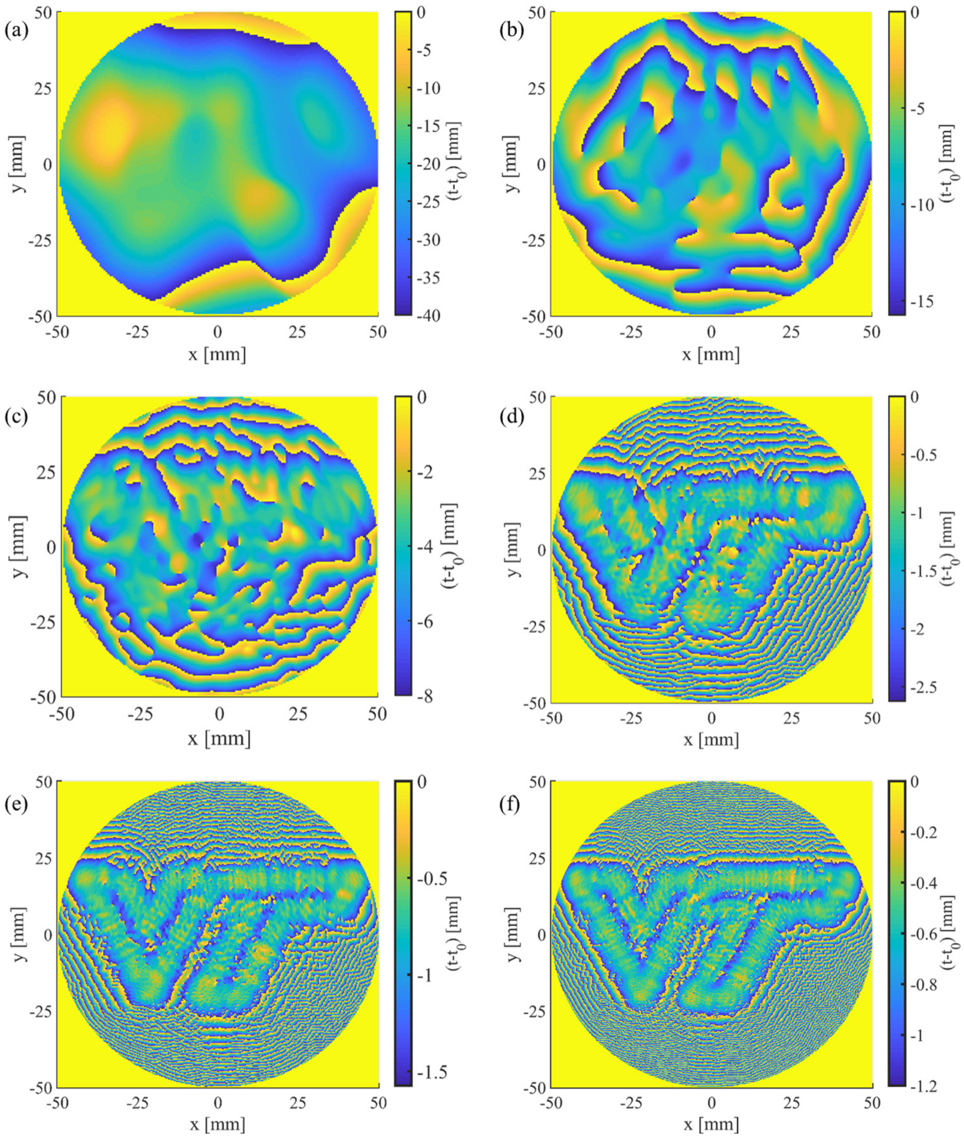

FIG. 6. Final thickness map of the hologram plate obtained from the IASA for excitation frequencies of (a) 100 kHz ($t_0 = 42$ mm), (b) 250 kHz ($t_0 = 17$ mm), (c) 500 kHz ($t_0 = 10$ mm), (d) 1.5 MHz ($t_0 = 5$ mm), (e) 2.5 MHz ($t_0 = 2$ mm), and (f) 3.3 MHz ($t_0 = 1.5$ mm).

requires a feasible computational time, is achieved. The number of pixels associated with the diffraction-limited acoustic hologram for the excitation frequency of 100 kHz are 161×161 with a resolution of $\lambda/24$ and the computational domain size is 481×481. For the frequencies of 1.5 MHz, 2.5 MHz, and 3.3 MHz, the hologram plane respectively comprises 301×301, 334×334, and 441×441 number of pixels and the computational domain size is 901×901, 1001×1001, and 1321×1321, respectively. The spatial sampling of $\lambda/3$ is used for the frequency of 1.5 MHz, and the frequencies of 2.5 MHz and 3.3 MHz are operated with the $\lambda/2$ sampling criteria. Other simulations are performed with the same number of hologram pixels and computational size as the one used for 1 MHz (Sec. III A). However, the resolution for driving frequencies of 250 kHz and 500 kHz are $\lambda/12$ and $\lambda/6$, respectively.

IV. EXPERIMENTAL RESULTS

A. Hologram fabrication and UAET experimental setup

The experiments were performed to show the functionality of the acoustic hologram in UAET. The hologram is designed, using the IASA algorithm, to generate a single acoustic focus on the left side of a target plane at a distance $z = 40$ mm from the hologram plane with the excitation frequency of 1 MHz. The focal area is defined to encompass a piezoelectric receiver disk, and after 60 iterations, the solution converges to the desired pressure pattern as shown in Fig. 7(a). The final thickness map, with an initial thickness of 5 mm, is presented in Fig. 7(b), which was rendered into a 3D-printed acoustic hologram using Clear Resin material with the properties described in Sec. III A. The UAET experimental setup with the acoustic hologram is shown in Fig. 8. The acoustic source (transmitter) is a PZT disk with a diameter of 50 mm and a thickness of 2.1 mm operating at the thickness mode of 1 MHz. We used two PZT receiver disks with a diameter of 19 mm, a thickness of 2 mm, and the resonance frequency (thickness mode) of 1 MHz and placed them in the target plane. All the disks are cylindrical 33-mode modified PZT-4 (Steiner & Martins, Inc.[62]), and the material properties are given by the manufacturer in Ref. 63. The hologram was mounted on the transmitter with a thin layer of high-shear-strength epoxy (3M DP460 Scotch-Weld Epoxy Adhesive).

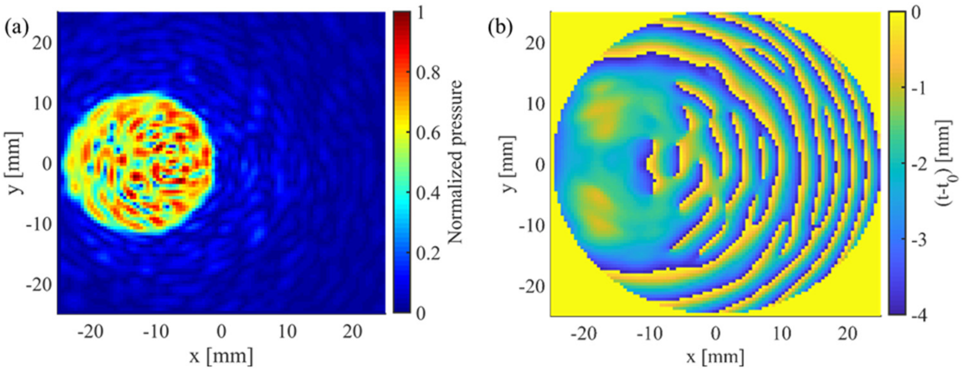

FIG. 7. (a) Normalized acoustic pressure distribution obtained from the IASA computational simulation in the target plane at $z = 40$ mm and (b) the corresponding final thickness map of the hologram plate. The driving frequency is 1 MHz.

The backside of the disks was fixed to fabricated acrylic holders using the same epoxy with the method described in Ref. 64.

The transmitter was actuated using a waveform generator (Keysight 33500B series) that was connected to an amplifier (Krohn-Hite Corp, model 7500). The receivers (R_1 and R_2 in Fig. 8) were connected to load resistors (RS-201W Wide-Range Precision Resistance Substituter) and a preamplifier (Stanford Research Systems Model SR560, Low-Noise Preamplifier) was used to amplify the receiver's signal. The data from the receivers was then acquired using NI SignalExpress® software through a National Instrument data acquisition device (PCI-6115). Furthermore, the data were bandpass filtered between 900 kHz and 1.1 MHz to reduce noise. The transmitter, hologram, and receivers were fully submerged in a $615 \times 318 \times 325\ \text{mm}^3$ tank of deionized water. Based on the desired pressure pattern from the acoustic holography [Fig. 7(a)], the voltage output from receiver R_1 was expected to be higher than that of receiver R_2. This outcome is illustrated in Sec. IV B.

B. Patterning in UAET using hologram: Pressure distribution and receivers' voltage response

The objective of the experiment is to excite the fixed-free receiver disks in the target plane by the transmitter and single acoustic hologram that were discussed above. The detailed theoretical modeling for longitudinal excitation of a fixed-free cylindrical piezoelectric receiver is described in Ref. 39, and the distributed-parameter solution of the closed-form voltage response is given in the supplementary material. We measured the sound pressure in the target plane at $z = 40$ mm using a calibrated 1 mm needle hydrophone (Precision Acoustics Ltd, with the sensitivity of 1154 mV/MPa at 1 MHz) mounted on a manufactured 3D positioning system. The hydrophone preamplifier was connected to a DC coupler with power supply (Precision Acoustics Ltd) referenced to the PCI-6115 card in which the hydrophone signal was acquired using a built-in MATLAB function (for data acquisition) and a developed script that 2D scans the acoustic field in the target plane. The data from hydrophone were also bandpass filtered between 900 kHz and 1.1 MHz. Figures 9(a) and 9(b) show

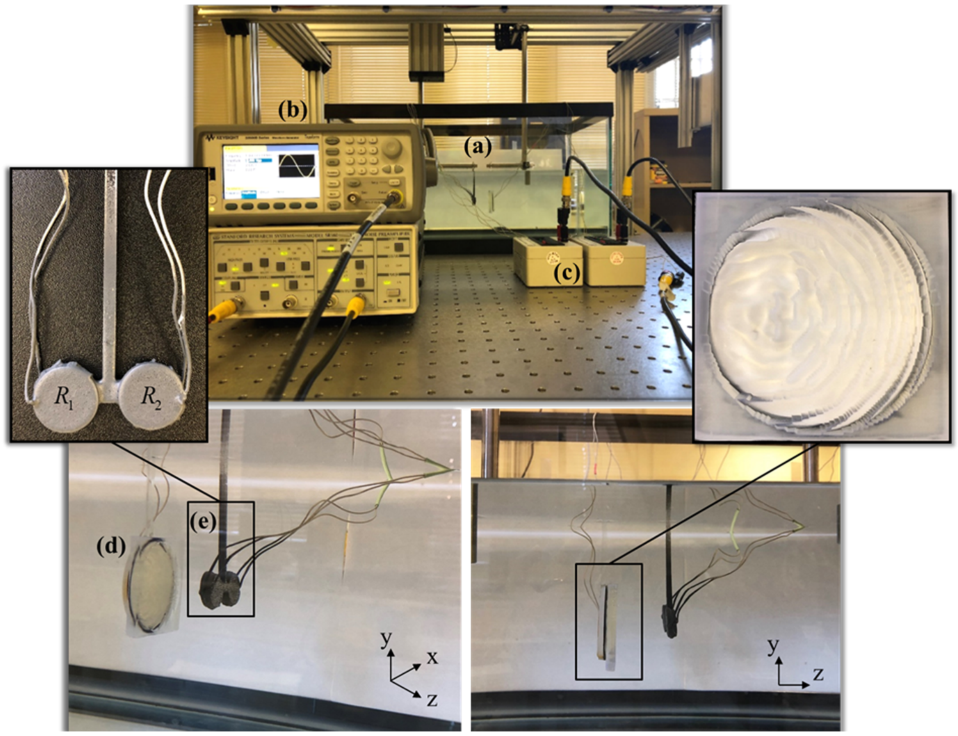

FIG. 8. Experimental setup showing the implementation of the acoustic hologram with the transmitter-receivers in UAET (a: deionized water tank, b: waveform generator and preamplifier, c: load resistors, d: transmitter and hologram, and e: receivers).

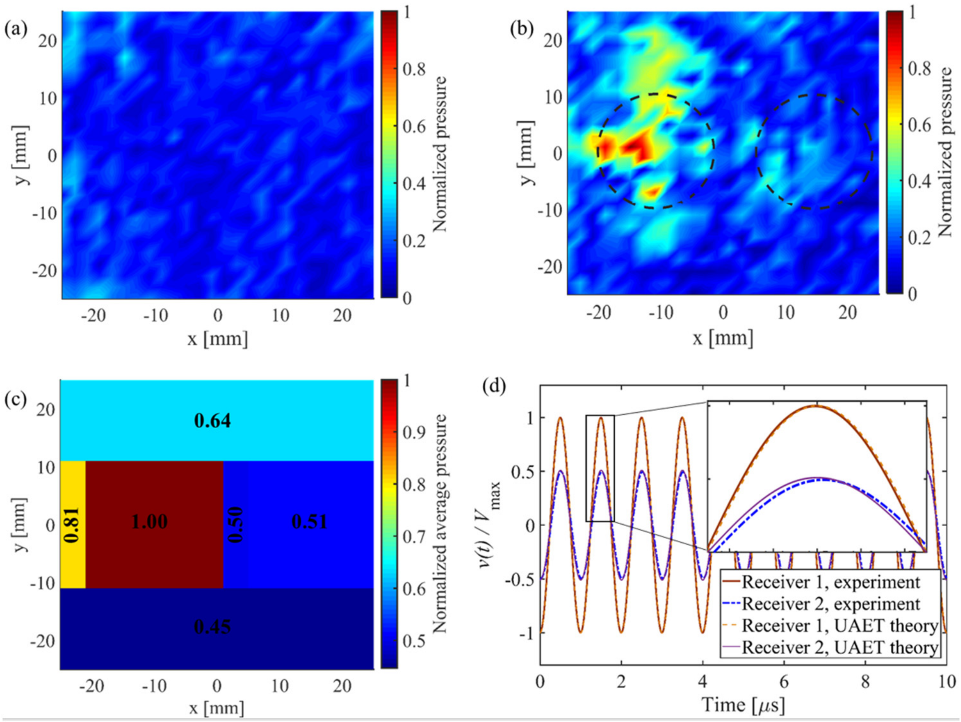

FIG. 9. Experimentally measured acoustic pressure distribution in the target plane at $z = 40$ mm: (a) when there is no hologram and (b) in the presence of the hologram. (c) The average pressure calculations (with the hologram) in defined segments and (d) the normalized experimentally measured voltage output from the two receivers located in the target plane compared with the UAET modeling results. The pressures and average pressures are normalized by the maximum value in (b) and (c), respectively. The driving frequency is 1 MHz.

the normalized peak pressure as measured by the hydrophone in the target plane when there is no acoustic hologram and in the presence of the hologram, respectively (see Fig. S2 in the supplementary material). Noticeably, using the acoustic hologram enhances the pressure amplitude in the targeted area and produces the focal point. Comparing the experimental results in the presence of the acoustic hologram [Fig. 9(b)] with the theoretical results [Fig. 7(a)], we observe a good agreement where the target pressure pattern (i.e., single desired focal point on the left side of the acoustic field) is clearly realized. Also, we have verified the functionality of the acoustic hologram in generating the patterned distribution of pressure at frequencies within ±20% of the operating frequency.

The dashed circles in Fig. 9(b) represent the locations of the PZT receivers in the target plane for the UAET experiment (see Fig. 8) and the normalized average pressure in the plot is calculated for the six selected segments of the field as shown in Fig. 9(c). Results presented in this section were verified in two ways. Firstly, we verified the functionality of the designed acoustic hologram using the IASA, in generating the patterned distribution of pressure by comparing Fig. 7(a) with Fig. 9(b). Secondly, we compared the time histories of the measured voltage output across the electrical load connected to the receivers with UAET modeling results for the PZT receivers excited by the given average pressure in Fig. 9(c). The average pressure in the segment including receiver 1 (R_1) is almost double ($1/0.51 = 1.96$) that of the receiver 2 (R_2), which means $p_t|_{\text{for R1}} = 1.96 p_t|_{\text{for R2}}$. Time histories of the measured voltage output across the electrical load connected to the receivers R_1 and R_2 are presented in Fig. 9(d). The ratio of the amplitudes of the voltage output is $v|_{\text{for R1}} = 2.02 v|_{\text{for R2}}$. A very good agreement is noted between these values and those predicted by the model in that the voltage response is linearly proportional to the input pressure as derived in Eq. (19), $v \propto p_t$. Hence, by using the designed acoustic hologram, a significant higher voltage output from R_1 is achieved, which shows the potential of the acoustic hologram in transferring localized and higher power to a receiver at the predetermined focal point.

V. CONCLUSIONS

Contactless ultrasonic power transfer is a promising approach for many potential applications such as wireless charging of medical implants used in therapy and sensor networks. One of the main challenges for ultrasonic acoustic energy transfer (UAET) is to desirably focus and pattern the transmitted energy and hence locally power wireless piezoelectric-based sensors. We investigated the use of acoustic holograms in UAET through which high amplitudes of acoustic pressure can be patterned to accomplish energy localization at predetermined focal points. An iterative angular spectrum approach was implemented to numerically design a metamaterial-based acoustic hologram for the reconstruction of the multi-focal pressure pattern. Further simulations were performed to analyze power transfer to multiple cylindrical receivers in a target plane. The results show that using the hologram in conjunction with UAET allows for enhanced and selective transfer of acoustic energy by taking advantage of beam steering and multi-focal patterning generated by the hologram. Effects of various parameters, such as operating frequency and hologram aperture size, on accuracy and quality of reconstruction of the desired pattern were investigated. It is shown that the performance quality and fidelity of the system are strongly affected by these parameters. The performed experiments show the potential of an acoustic hologram in constructing a single acoustic focus to selectively transmit energy to a receiver located at a predetermined focal point with dramatic power output enhancement.

SUPPLEMENTARY MATERIAL

The supplementary material includes a more detailed analysis of transmission coefficient for three layers, where one of them is an acoustic hologram, pictures of the experimental setup showing hydrophone measurements, and the distributed-parameter solution of the closed-form voltage response for a fixed-free cylindrical piezoelectric receiver.

ACKNOWLEDGMENTS

This work was supported by the National Science Foundation (NSF) (Grant No. ECCS-1711139), which is gratefully acknowledged. The authors would also like to thank Omidreza Sadeghi for helping with experiments.

[1] J. Castle, M. Butts, A. Healey, K. Kent, M. Marino, and S. B. Feinstein, Am. J. Physiol. Heart Circ. Physiol. **304**, H350 (2012).
[2] W. G. Pitt, G. A. Husseini, and B. J. Staples, Expert Opin. Drug Deliv. **1**, 37 (2004).
[3] K. K. Shung, *Diagnostic Ultrasound: Imaging and Blood Flow Measurements* (CRC Press, 2015).
[4] M. G. Roes, J. L. Duarte, M. A. Hendrix, and E. A. Lomonova, IEEE Trans. Ind. Electron. **60**, 242 (2013).
[5] M. A. Andrade, N. Pérez, and J. C. Adamowski, Appl. Phys. Lett. **106**, 014101 (2015).
[6] P. Glynne-Jones, R. J. Boltryk, and M. Hill, Lab. Chip **12**, 1417 (2012).
[7] A. Marzo, S. A. Seah, B. W. Drinkwater, D. R. Sahoo, B. Long, and S. Subramanian, Nat. Commun. **6**, 8661 (2015).
[8] Y. Hertzberg and G. Navon, Med. Phys. **38**, 6407 (2011).
[9] T. L. Szabo, *Diagnostic Ultrasound Imaging: Inside Out* (Academic Press, 2004).
[10] F. Dunn, W. Hartmann, D. Campbell, and N. H. Fletcher, *Springer Handbook of Acoustics* (Springer, 2015).
[11] Y. Tian, Q. Wei, Y. Cheng, and X. Liu, Appl. Phys. Lett. **110**, 191901 (2017).
[12] Y. Xie, W. Wang, H. Chen, A. Konneker, B.-I. Popa, and S. A. Cummer, Nat. Commun. **5**, 5553 (2014).
[13] N. J. Gerard, Y. Li, and Y. Jing, J. Appl. Phys. **123**, 124905 (2018).
[14] Y. Li, X. Jiang, B. Liang, J.-c. Cheng, and L. Zhang, Phys. Rev. Appl. **4**, 024003 (2015).
[15] S. Qi, Y. Li, and B. Assouar, Phys. Rev. Appl. **7**, 054006 (2017).
[16] W. Tang and C. Ren, J. Phys. D Appl. Phys. **50**, 425104 (2017).
[17] B. Yuan, Y. Cheng, and X. Liu, Appl. Phys. Express **8**, 027301 (2015).
[18] Y. Li, B. Liang, Z.-m. Gu, X.-y. Zou, and J.-c. Cheng, Sci. Rep. **3**, 2546 (2013).
[19] Y. Xie, C. Shen, W. Wang, J. Li, D. Suo, B.-I. Popa, Y. Jing, and S. A. Cummer, Sci. Rep. **6**, 35437 (2016).
[20] Y. Zhu, J. Hu, X. Fan, J. Yang, B. Liang, X. Zhu, and J. Cheng, Nat. Commun. **9**, 1632 (2018).
[21] B. Liu, B. Ren, J. Zhao, X. Xu, Y. Feng, W. Zhao, and Y. Jiang, Appl. Phys. Lett. **111**, 221602 (2017).
[22] Y. Xie, A. Konneker, B.-I. Popa, and S. A. Cummer, Appl. Phys. Lett. **103**, 201906 (2013).
[23] S.-Y. Zuo, Y. Tian, Q. Wei, Y. Cheng, and X.-J. Liu, J. Appl. Phys. **123**, 091704 (2018).
[24] S. Zhang, C. Xia, and N. Fang, Phys. Rev. Lett. **106**, 024301 (2011).
[25] K. Melde, A. G. Mark, T. Qiu, and P. Fischer, Nature **537**, 518 (2016).
[26] M. D. Brown, B. T. Cox, and B. E. Treeby, Appl. Phys. Lett. **111**, 244101 (2017).
[27] M. Brown, D. Nikitichev, B. Treeby, and B. Cox, Appl. Phys. Lett. **110**, 094102 (2017).
[28] M. D. Brown, J. Jaros, B. T. Cox, and B. E. Treeby, J. Acoust. Soc. Am. **139**, 1637 (2016).
[29] M. D. Brown, E. Martin, B. T. Cox, and B. E. Treeby, in *Single Pulse Illumination of Multi-Layer Photoacoustic Holograms for Patterned Ultrasound Field Generation* (IEEE, 2016), p. 1.
[30] S. Yoshizawa, T. Ikeda, A. Ito, R. Ota, S. Takagi, and Y. Matsumoto, Med. Biol. Eng. Comput. **47**, 851 (2009).
[31] I. F. Akyildiz, W. Su, Y. Sankarasubramaniam, and E. Cayirci, Comput. Netw. **38**, 393 (2002).
[32] D. Seo, J. M. Carmena, J. M. Rabaey, M. M. Maharbiz, and E. Alon, J. Neurosci. Methods **244**, 114 (2015).
[33] G. ter Haar and C. Coussios, Int. J. Hypertherm. **23**, 89 (2007).
[34] S. Shahab, M. Gray, and A. Erturk, J. Appl. Phys. **117**, 104903 (2015).
[35] M. Carrara, M. Cacan, M. Leamy, M. Ruzzene, and A. Erturk, Appl. Phys. Lett. **100**, 204105 (2012).
[36] M. Carrara, J. Kulpe, S. Leadenham, M. Leamy, and A. Erturk, Appl. Phys. Lett. **106**, 013907 (2015).
[37] D. Shmilovitz, S. Ozeri, C.-C. Wang, and B. Spivak, IEEE Trans. Biomed. Eng. **61**, 995 (2014).
[38] S. D. Mellin and G. P. Nordin, Opt. Express **8**, 705 (2001).
[39] S. Shahab and A. Erturk, Smart Mater. Struct. **23**, 125032 (2014).
[40] R. Hill and S. M. El-Dardiry, J. Acoust. Soc. Am. **67**, 673 (1980).
[41] E. K. Lawrence, R. F. Austin, B. C. Alan, and V. S. James, *Fundamentals of Acoustics* (John Wiley, New York, 2000), p. 169.
[42] R. J. McGough, J. Acoust. Soc. Am. **115**, 1934 (2004).
[43] X. Zeng and R. J. McGough, J. Acoust. Soc. Am. **123**, 68 (2008).
[44] J. W. Goodman, *Introduction to Fourier Optics* (Roberts and Company Publishers, 2005).
[45] J. F. Kelly and R. J. McGough, IEEE Trans. Ultrason. Ferroelectr. Freq. Control **53**, 1150 (2006).
[46] E. G. Williams, *Fourier Acoustics: Sound Radiation and Nearfield Acoustical Holography* (Academic Press, 1999).
[47] D.-L. Liu and R. C. Waag, IEEE Trans. Ultrason. Ferroelectr. Freq. Control **44**, 1 (1997).
[48] E. F. Grande and F. Jacobsen, Ph.D. thesis, Department of Electrical Engineering, Technical University of Denmark (DTU), 2012.
[49] F. Jacobsen, G. Moreno-Pescador, E. Fernandez-Grande, and J. Hald, J. Acoust. Soc. Am. **129**, 3461 (2011).
[50] W. Veronesi and J. D. Maynard, J. Acoust. Soc. Am. **81**, 1307 (1987).
[51] J. D. Maynard, E. G. Williams, and Y. Lee, J. Acoust. Soc. Am. **78**, 1395 (1985).
[52] E. G. Williams and J. Maynard, Phys. Rev. Lett. **45**, 554 (1980).
[53] S. Shahab, M. Gray, and A. Erturk, in *An Experimentally Validated Contactless Acoustic Energy Transfer Model with Resistive-Reactive Electrical Loading* (International Society for Optics and Photonics, 2015), p. 943105.
[54] J. L. Butler and C. H. Sherman, *Transducers and Arrays for Underwater Sound* (Springer, 2016).
[55] A. Erturk and D. J. Inman, *Piezoelectric Energy Harvesting* (John Wiley & Sons, 2011).
[56] See https://www.piceramic.com/en/company/ for the company info.
[57] See https://www.piceramic.com/en/products/piezoceramic-materials/ for the material properties.
[58] M. Bakhtiari-Nejad, A. Elnahhas, M. R. Hajj, and S. Shahab, in *Passive Metamaterial-Based Acoustic Holograms in Ultrasound Energy Transfer Systems* (International Society for Optics and Photonics, 2018), p. 1059518.
[59] D. Callens, C. Bruneel, and J. Assaad, NDT E Int. **37**, 591 (2004).
[60] G. H. Koopmann, L. Song, and J. B. Fahnline, J. Acoust. Soc. Am. **86**, 2433 (1989).
[61] A. Sarkissian, J. Acoust. Soc. Am. **118**, 671 (2005).
[62] See https://www.steminc.com/PZT/ for the company info.
[63] See http://www.steminc.com/piezo/PZ_property.asp for the material properties.
[64] S. Anton, A. Erturk, and D. Inman, Smart Mater. Struct. **19**, 115021 (2010).